# Reverse Engineering and Improvement of the FCX24 Lemur RC Car

Injae JunJinsuh LeeYeongrok ChoiDoyeon ParkJiyong KimWonjae Kim

#### I. Introduction

Automobiles play an indispensable role in our daily lives, not only as a means of transportation but also as a subject of engineering interest. In this regard, RC cars offer a unique blend of realistic mechanical structures and dynamic interactivity. Their compact size, yet functional resemblance to real vehicles, makes them ideal candidates for mechanical analysis and performance studies.

For this analysis, we selected the FMS 1:24 FCX24 Lemur RTR RC car (Fig. 1). It is remotely controlled via wireless communication and scaled down to approximately 90% of the size of a full-sized vehicle. Despite its small size, this model accurately replicates key systems of actual automobiles, including suspension, transmission, chassis, drivetrain, and steering mechanisms. Therefore, by analyzing this model, we aim to gain a deeper understanding of real vehicle components and driving mechanisms and ultimately propose improvements from a vehicle dynamics perspective.

#### A. Reasons of Selection

First, as mentioned above, RC cars share many functional similarities with real automobiles, offering a wide range of elements that can be analyzed from various branches of mechanics.

From a solid mechanics perspective, we can study the structural effectiveness of the trapezoidal beam frame in protecting internal components and passengers during collisions. From a dynamic perspective, we can analyze how motor power is transmitted through the drivetrain to the wheels, and how the transmission changes gear ratios to provide torque and RPM suited to different driving conditions.

Second, analyzing a full-scale vehicle is extremely costly and logistically challenging. In contrast, studying an RC car (which shares many of the same mechanical principles and components) is far more cost-effective and accessible. While there are undeniable differences in the drivetrain systems between RC cars and real vehicles, analyzing components such as gears, drivetrain and suspension systems still offers valuable insights into overall vehicle performance from a mechanical engineering perspective.

Lastly, the wide availability of RC car models on the market provides a diverse range of options. Among these, we selected the FCX24 Lemur because it features a two-speed transmission system (an uncommon characteristic among RC cars in the same price range) which makes it particularly interesting for analysis (Fig. 2).

#### B. Comparison of FCX24 Lemur RC Car with two Similar Products

F1 race cars, like RC cars, are high-tech vehicles with similar mechanical structures. Both allow easy modification, and unlike regular cars, their components are designed for quick attachment and removal (Fig. 3), making full-vehicle analysis more accessible.

Miniature cooking and RC cars share surprising similarities, as both involve small-scale replicas that closely mimic real-world counterparts (Fig. 4). While miniature cooking uses tiny yet functional tools, RC cars incorporate detailed components like engines, suspensions, and tires. Both captivate audiences through their realism and intricate craftsmanship.

# II. FCX24 Lemur RC Car Description

#### A. Description and External Analysis

Our RC car, the FCX24 Lemur, is composed of several key subsystems that closely resemble those of a real vehicle. These include the chassis, powertrain, steering mechanism, suspension system, and body frame with external features.

The chassis is constructed from high-strength nylon, which offers greater strength and reduced weight compared to traditional ladder frame designs that use metal side beams and plastic trusses. This lightweight yet durable structure forms the backbone of the vehicle (Fig. 5).

At the core of the powertrain is a centrally mounted 130 brushed motor powered by a rear battery. Its mid-mount layout lowers the center of gravity and improves stability. Integrated with a two-speed transmission and transfer case, it delivers power to all four wheels via universal joint drive shafts; ideal for off-road conditions (Fig. 6).

The steering system consists of a front-mounted servo motor connected to a two-bar linkage. When actuated, the linkage rotates to steer the front wheels left or right. A spring is installed to prevent the linkage from overextending during operation (Fig. 7).

The suspension system uses high-mounted links and a raised frame for better obstacle clearance. Tuned coil springs and dampers reduce roll, while independent front and rear wheel movement maintains ground contact on uneven terrain, enhancing traction and ride comfort (Fig. 8).

Externally, the bumper is a dual-tube design made of two parallel bars, functioning as a primary shock absorber during frontal collisions. It reduces the direct transmission of impact forces to the chassis (Fig. 9).

The vehicle measures  $209 \text{ mm} \times 128 \text{ mm} \times 120 \text{ mm}$ , with a 136 mm wheelbase and 66 mm diameter tires. The center of gravity, determined from the tipping point, is 108 mm from the front bumper, 43 mm above the ground, and laterally centered (Fig. 10). Though relatively high, the mid-mounted motor and four-wheel drive help maintain stability during motion.

#### B. Driving Performance Analysis: Speed and Climbing Ability

In low gear, although the speed is slow (Fig. 11), the high torque provides strong power (Fig. 13). As seen in the video, this allows for stable driving and precise control on rough or inclined terrain. However, due to the low speed (Fig. 12), it is inefficient for long-distance driving.

In high gear, the vehicle moves faster, but the torque is lower, resulting in weaker force. On slippery surfaces, rough terrain, or inclines, it becomes harder to control—frequent slipping, bouncing, or even flipping can occur (Fig. 14).

With low gear, the vehicle can stably climb over obstacles even with relatively low output (Fig. 15). However, in high gear, if the output is low, it fails to climb, and the wheels spin out (Fig. 16). Increasing the output slightly may help it climb, but the lack of control at high speeds leads to instability, such as flipping or rolling over.

## III. Disassembly and Analysis

As mentioned in the introduction, one of the key advantages of our RC car is that nearly all of its components are easy to disassemble and reassemble. The frame, drivetrain, and even the motor are all secured using hex socket bolts. Due to the compact size of the car, the bolts are also correspondingly small and can be removed with a 1.5 mm hex wrench: the smallest commonly available size (Fig. 17).

Upon complete disassembly, we found that the car consists of numerous individual components, which can be broadly categorized into the following systems: power source, drivetrain, steering system, chassis, suspension, and additional electronic components (Fig. 18).

### A. Overview of Auxiliary Components

The vehicle also includes several auxiliary components. Inside the trunk is a 2S LiPo 7.4V 380mAh battery, which supplies power to the ESC group control board via a battery switch. This control board manages motor RPM and steering during operation. Additionally, the vehicle is equipped with headlights to enable driving in low-light or night-time conditions.

Four tires were attached to the axle with a fixed nut to a nut-shaped hole to prevent slippage while in action. The key element to fix the nut to the shaft is shown in the following figure (Fig. 19). Also, the tires lack inflation and are quite light weighted compared to real car tires (Fig. 20). This provides the advantage of allowing the tires to flex and adapt to the terrain, but the low friction can lead to slippage when driving over rough or uneven surfaces.

#### **B. Detailed Analysis of Core Mechanical Systems**

#### Chassis

The chassis is the vehicle's structural backbone, connecting major systems like the drivetrain, suspension, and steering. It must endure impacts, vibrations, and load transfers. Identifying stress concentrations under various loads is essential for detecting weak points and informing structural improvements.

To explore these stress concentrations in detail, this section presents the analysis of the chassis truss under external loads using Fusion 360's static load simulation. A replicated linkage model was constructed with two end plates and boundary conditions to simulate the chassis being fixed to the plates.

Results for horizontal and vertical loading are shown in (Fig. 21) and (Fig. 22), respectively. Under horizontal loading, high stress concentrations appear in regions 1, 2, and 3. Regions 1 and 2 are affected by deflection in the X-Y plane due to the truss not being strictly aligned with the Y-Z axis, leading to buckling-like stress. Region 3 shows high stress due to proximity to the loading point.

Under vertical loading in (Fig. 22), the upper ceiling area of the chassis bears the load effectively, indicating good vertical load distribution.

The yield strength of ABS plastic is about 40 MPa. Some small regions with highly complex geometry showed unrealistic stress peaks (e.g., over 100 MPa), which are attributed to CAD model limitations. Excluding these anomalies, most of the structure remained within the material's yield range. Thus, the chassis is estimated to withstand approximately 100 N horizontally and 250 N vertically without failure.

Because RC cars rarely face such big static loads in real-life, we used ANSYS Explicit Dynamics to better simulate real-world collision scenarios [1] [2]. (Fig. 23) and (Fig. 24) show the simulation results. The chassis velocity was set to 4m/s, with the wall material modeled as concrete and the chassis as ABS plastic. The maximum Equivalent von-Mises stress is about 600MPa following (Fig. 23). Considering that the UTS of ABS plastic is about 40Mpa, plastic deformation is expected. But by following (Fig. 24), total deformation appears minimal that it is barely recognized on the color bar.

Nonetheless, the reliability of this simulation is limited due to the difficulty of accurate modeling CAD, which led to several improvised modifications [3]. The cone-like mesh right in front of the wall represents this error: it was not included in real life and in the original CAD version. But the maximum speed of the RC car is 2.22m/s- much slower than the simulated speed(4m/s) and considering that real RC cars are more robust against impact stresses, we conclude that RC cars are safe enough under its own driving condition.

#### **Drivetrain and Transmission**

The drivetrain and transmission are essential for delivering motor power to the wheels and controlling torque and speed through gear shifting. In particular, the two-speed transmission allows the vehicle to switch between high-torque low-speed and high-speed low-torque modes, adapting to different driving conditions. This analysis focuses on disassembling the gear system

to evaluate gear ratios, torque transmission, and RPM behavior in both modes, providing insight into the performance and versatility of the RC car's powertrain.

The gearbox consists of the following components: motor, low-speed gear, high-speed gear, and a shifter [4] for gear switching. We numbered the gears sequentially starting from gear (1) directly connected to the motor (Fig. 25) and measured the diameter of each gear (see table). For both high-gear and low-gear configurations, we identified the gear engagement sequence and calculated the corresponding RPM ratios (Table. 1) [5]. In both modes, the gear sequence is identical up to gear (3-1), after which the power transmission path diverges due to the action of the shifter (Table. 2) (Table. 3).

Based on this mechanism, the RPM ratios for the vehicle's drivetrain under both gear modes were calculated.

$$rpm_{high} = 1 * \frac{1}{N_{1,2-1}} * 1 * \frac{1}{N_{2-2,3-1}} * \frac{1}{N_{3-1,4}} = 1 * \frac{7}{27} * 1 * \frac{7}{13} * 1 = 0.140$$

$$rpm_{low} = 1 * \frac{1}{N_{1,2-1}} * 1 * \frac{1}{N_{2-2,3-1}} * 1 * \frac{1}{N_{3-2,5-1}} * 1 * \frac{1}{N_{5-2,6}} * \frac{1}{N_{6,7}}$$

$$= 1 * \frac{7}{27} * 1 * \frac{7}{13} * 1 * \frac{7}{13} * 1 * \frac{7}{13} * 1 = 0.040$$
(2)

The RPM values were calculated as relative ratios [6], based on the assumption that the motor rotates once (i.e., motor RPM = 1). The final gear that delivers torque to the drive shaft was then analyzed to determine how many times it rotates relative to the motor. This is why the initial term in equations (1) and (2) is set to 1.

Although the gear pairs—Gear 2-1 and 2-2, Gear 3-1 and 3-2, and Gear 5-1 and 5-2—have different diameters and gear ratios, each pair rotates as a single rigid body. Therefore, a factor of 1 was applied when calculating the overall RPM ratio.

The results show that when the motor completes one full rotation, the final gear in the high-speed gear path rotates 0.14 turns, while the final gear in the low-speed gear path rotates 0.04 turns. From this, we can deduce that the high-speed gear configuration produces an RPM that is 3.5 times greater than that of the low-speed gear.

Next, we calculated the torque transmitted to the drive shaft relative to the motor's input torque. Let T<sub>1</sub> represent the motor's input torque. Since the gearbox is composed of spur gears, we assumed a mechanical efficiency of 98% for each gear stage [7].

$$T_{high} = 1 * N_{1,2-1} * 1 * N_{2-2,3-1} * N_{3-1,4} * 0.98^{3} * T_{1}$$

$$= 1 * \frac{27}{7} * 1 * \frac{13}{7} * 1 * 0.98^{3} * T_{1} = 6.742T_{1}$$

$$T_{low} = 1 * N_{1,2-1} * 1 * N_{2-2,3-1} * 1 * N_{3-2,5-1} * 1 * N_{5-2,6} * N_{6,7} * 0.98^{5} * T_{1}$$

$$= 1 * \frac{27}{7} * 1 * \frac{13}{7} * 1 * \frac{13}{7} * 1 * \frac{13}{7} * 1 * 0.98^{5} * T_{1} = 22.332T_{1}$$

$$(4)$$

In high-speed mode, the output torque is 6.742 times the input torque, while in low-speed mode, the output torque reaches 22.332 times the input torque. This indicates that the low-speed output torque is approximately 3.31 times greater than the high-speed output torque. Considering that, as previously discussed, the RPM in high-speed mode is about 3.5 times that of low-speed mode, this confirms the inverse relationship between torque and RPM.

Minor discrepancies between the theoretical ratio and calculated results can be attributed to friction between gears and energy loss due to the moment of inertia of the rotating components. This is the reason we included exponential factors of 0.98 in equations (3) and (4) to account for efficiency loss at each gear stage.

Finally, the gear shifting mechanism was examined. Inside the gearbox, shifting is performed by a shifter, a mechanical component that physically pushes or pulls the shift gear into engagement with either the low-speed or high-speed gear set. As shown in Figure N, a servo

motor located outside the gearbox actuates the shift fork by sliding laterally. The shift fork then moves a hexagonal gear, causing it to mesh with either the low or high gear.

When the hexagonal gear engages with the low-speed gear, the vehicle enters low-speed mode; conversely, when it engages with the high-speed gear, the vehicle switches to high-speed mode.

#### **Steering System**

The steering system is essential for controlling direction and maneuverability, particularly on rough terrain. In off-road RC cars, their responsiveness and structure directly affect performance and stability. Understanding how motion is transmitted from the servo motor to the wheels, along with key parameters like steering ratio and linkage geometry, is crucial for evaluating and improving steering behavior.

FCX24 Lemur's steering system operates based on a single servo motor mounted at the front of the vehicle (Fig. 26). The rotational motion of the servo motor is transmitted to the front wheels through a 2-bar linkage system as demonstrated in the video (Fig. 27). As the linkage extends or contracts in response to the servo motor's rotation, the direction of the front wheels changes accordingly to the left or right.

The steering system of the RC car is designed to automatically return the front wheels to their neutral, center-aligned position when the controller wheel is released. This mechanism relies on the interaction between the servo motor and a helically contoured (spiral-like) steering linkage, as shown in (Fig. 28) and (Fig. 29). When the servo motor rotates, it not only pivots the linkage but also pushes it forward due to its twisted geometry. This action compresses an integrated spring in the system. Once the user releases the steering input on the controller, the restoring force of the spring causes the linkage and front wheels to return to their original neutral position as shown in the video (Fig. 30). This self-centering mechanism enhances user control, enabling quick and intuitive steering corrections even from a distance.

To analyze how the responsiveness of the RC car's steering system directly affects driving performance, stability, and obstacle handling, we calculated the response time and steering ratio through the following steps.

Based on the definition of the steering ratio, which represents the relationship between input motion and wheel turning angle, we can understand how it influences the vehicle's steering sensitivity and controllability: making its analysis essential for optimizing maneuverability.

The torque and response time of the servo motor were obtained from the motor's specification sheet [8].

$$\tau_{servo} = 2.5 \ kg \cdot cm = 0.2452 \ N \cdot m, \quad \omega = \frac{60^{\circ}}{0.12s} \approx 8.73 \ rad/s$$

The geometry of the 2-bar linkage was measured as follows (Fig. 31):

$$r_{servo-arm} = 0.015 m$$
, Distance to the center of the tie lod  $L_t = 0.030 m$ 

The maximum rotation angle of the servo motor was found to be  $\theta_{\text{servo,max}} = 30^{\circ}$ , and given the measured angular velocity, it achieves full deflection in just 0.06 seconds, demonstrating rapid and immediate responsiveness.

The steering angle and steering ratio were measured as follows:

Steering Angle 
$$\theta_{wheel} = \arcsin\left(\frac{r_{servo-arm} \times \sin(\theta_{servo,max})}{L_t}\right) = 14.48^{\circ}$$
Steering Ratio  $\frac{30^{\circ}}{14.48^{\circ}} = 2.072$ 

The RC car has a very low steering ratio of approximately 2.07, which according to (Table. 4), results in highly responsive steering [9]. This is advantageous for off-road driving, as it allows quick directional changes and helps the vehicle overcome obstacles. However, it also leads to instability at high speeds. Since this RC car model is designed for off-road use, the low steering ratio is appropriate for navigating rough terrain, but it becomes unstable during high-speed driving.

#### Suspension

In a vehicle's suspension system, the spring functions to absorb shocks from uneven terrain by storing and releasing mechanical energy, while the damper (or shock absorber) dissipates this energy to reduce oscillations and maintain vehicle stability.

Based on this understanding, we conducted an analysis to determine whether the suspension system of the FCX24 Lemur provides appropriate damping and stiffness values to enhance driving stability.

The suspension system, shown in (Fig. 32), includes key components such as the spring, shock shaft, cylinder body, and O-ring. Spring absorbs shocks, while the shock shaft and cylinder dampen motion. The O-ring prevents leakage and ensures smooth operation. Together, they reduce vibrations and help maintain tire contact for stable driving.

We focused our analysis on a single suspension system (Fig. 33), as the vehicle's weight was previously confirmed to be evenly distributed across all four suspension units based on the measured center of gravity. As shown in the diagram, the system was modeled as a series connection of two springs and one damper, where the tire itself was also treated as a spring component (Fig. 34), following modeling approaches referenced in the literature (Fig. 35)(Fig. 36) [14].

The system includes a wheel spring with stiffness constant  $k_1$ , and a triangular link structure that connects a spring-damper assembly characterized by stiffness  $k_2$  and damping coefficient  $c_0$  to the wheel hub. Due to lateral symmetry, horizontal motion is constrained, allowing the model to focus solely on vertical dynamics [10]. Additionally, it is assumed that the entire mass of the vehicle body is concentrated at the top of the system, designated as point E, with a total mass of m. Based on these assumptions, the system is represented by a four-degree-of-freedom (4-DOF) equation of motion [11].

$$\begin{bmatrix} 0 & -\sin(\varphi) & 0 & k_2 \\ 0 & m\cos(\varphi) & -mL\sin(\varphi) & \cos(\varphi) \\ m & m\sin(\varphi) & mL\cos(\varphi) & \sin(\varphi) \\ 0 & -k_1 & 0 & 1 \end{bmatrix} \begin{bmatrix} \ddot{R} \\ \ddot{L} \\ \ddot{\varphi} \\ T \end{bmatrix} = \begin{bmatrix} 0 \\ 2m\dot{L}\dot{\varphi}\sin(\varphi) + mL\dot{\varphi}^2\cos(\varphi) \\ -2m\dot{L}\dot{\varphi}\cos(\varphi) + mL\dot{\varphi}^2\sin(\varphi) - F(t) \\ -c_0\dot{L} \end{bmatrix}$$
(5)

The equation derived above is somewhat complex for direct analysis, so an additional assumption is introduced to simplify the system. Assuming small displacements, the spring-damper assembly is considered to maintain a fixed angle of  $80^{\circ}$  with respect to the ground. Based on this assumption, a reduced two-degree-of-freedom (2-DOF) model is derived, referred to as the "Small Motion, Fixed  $80^{\circ}$ " model. In this formulation, point A is defined as the origin. The position of point D is given by (c, R + d + y), and the position of point E is defined as  $(c + (L_0 + x)cos\theta, R + d + y + (L_0 + x)sin\theta)$ , where c = 8.5 mm and d = 5.7 mm.

$$\begin{cases}
 m(\ddot{y} + \ddot{x}\sin\theta) + k_2 y = F(t) \\
 m(\ddot{x} + \ddot{y}\sin\theta) + c_0 \dot{x} + k_1 x = F(t)\sin\theta
\end{cases} (\theta = 80^\circ)$$
(6)

To calculate the parameters in the above equation, the stiffness values (k) of the tire and spring were obtained through force–displacement measurements (Fig. 37). The damping coefficient (c) was determined by plotting force–velocity characteristics, using a Zaber actuator and a Mark-10 force sensor while pulling the damper at various speeds (Fig. 38). The experimentally measured values were  $k_1 = 2141 \text{ N/m}$ ,  $k_2 = 87.77 \text{ N/m}$ , and  $c_0 = 20 \text{ Ns/m}$ .

The detailed computational steps for Equation (6) are provided in the appendix (3.1). An analysis was performed on the vibrational response immediately following a 5 cm drop impact [12]. The results are shown in (Fig. 39)(Fig. 40)(Fig. 41), with further interpretation summarized in (Table. 5).

Overall, both the overshoot and settling time satisfied established engineering guidelines [13], indicating that the suspension system of the FCX24 Lemur is well-optimized for impact absorption and dynamic stability.

## IV. Improvement Suggestion and Testing

#### Variable Steering Ratio System

As analyzed above, the FCX24 Lemur has a very low steering ratio of approximately 2.07, which results in highly responsive steering; ideal for off-road driving but prone to instability at high speeds. To address this trade-off between agility and stability, the steering ratio could be dynamically adjusted based on driving conditions.

A Variable Steering Ratio (VSR) System dynamically adjusts the steering ratio based on factors like vehicle speed and steering input. Unlike traditional systems with a fixed ratio, VSR reduces the ratio at low speeds for quick, tight turns and increases it at high speeds for greater stability. This improves both low-speed maneuverability and high-speed safety. VSR is typically implemented through electric power steering with sensors and control units, and is used by brands like BMW, Mercedes-Benz, and Lexus. Similar concepts can be applied to RC cars using variable servo control based on speed or position, enhancing both agility and control.

#### **Preventing Rear Wheel Slip**

As shown in (Fig. 16), rear-wheel slip occurred while climbing an incline. To address this issue, it is necessary to increase the load on the rear wheels. We propose increasing the total vehicle weight to 500 g and repositioning heavy components such as the main motor toward the rear, so that approximately 60% of the total load is distributed to the rear axle.

Following this modification, new values for the spring constant (k) and damping coefficient (c) were recalculated using Equation (6) to achieve critical damping under the updated weight distribution. To realize the required damping coefficient, we first identified the target kinematic viscosity of the suspension oil. To achieve this viscosity, we calculated the appropriate mixing ratio of two oils with different viscosities. A damper was fabricated based on the computed ratio, and its actual damping coefficient was measured and compared with the theoretical value.

After adjusting the vehicle mass and center of gravity, the newly calculated parameters for critical damping were  $k_1 = 150$  N/m and  $c_0 = 18$  Ns/m. The dynamic viscosity corresponding to this damping coefficient was computed using a flow rate–pressure drop relationship. Subsequently, the oil density was measured, and the kinematic viscosity was derived. Full details of the calculation procedure are provided in the (3.2). As a result, the required oil viscosity was determined to be 2010 cSt.

To produce this viscosity, a mixture of 100 cSt and 11,000 cSt suspension oils was used (Fig. 42). The precise mixing ratio was calculated using the following equation:

$$\begin{aligned} log_{10}(v_{blend}) &= xlog_{10}(v_1) + (1-x)log_{10}(v_2) \\ v_1 &= 100cSt, v_2 = 11000cSt, v_{blend} = 2010cSt \\ x &= 0.36 \end{aligned}$$

Using the calculated ratio, the two oils were mixed to fabricate the damper, and the forcevelocity characteristics were measured using the same method as before with the Zaber actuator and Mark-10 force sensor (Fig. 43). The resulting damping coefficient was measured to be 18.83 Ns/m, which corresponds to a 4.6% deviation from the target value of 18 Ns/m. With this custom-fabricated suspension system and the adjusted vehicle weight and center of gravity, we expect a significant reduction in rear-wheel slip.

# Appendix

# 1. Figures



Fig. 1. RC car (FMS 1:24 FCX24 Lemur RTR)

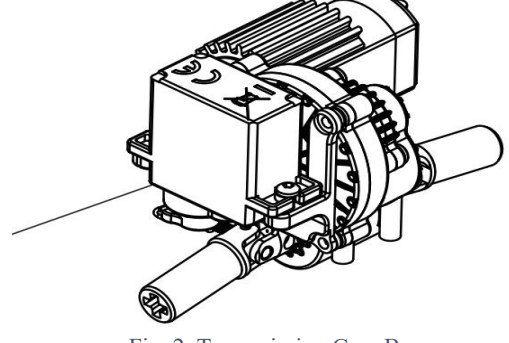


Fig. 2. Transmission Gear Box



Fig. 3. F1 pit stop



Fig. 4. Miniature Cooking Set



Fig. 5. Chassis and Overall Structure



Fig. 6. Powertrain (video)





Fig. 7. Steering System (video)



Fig. 9. Bumper

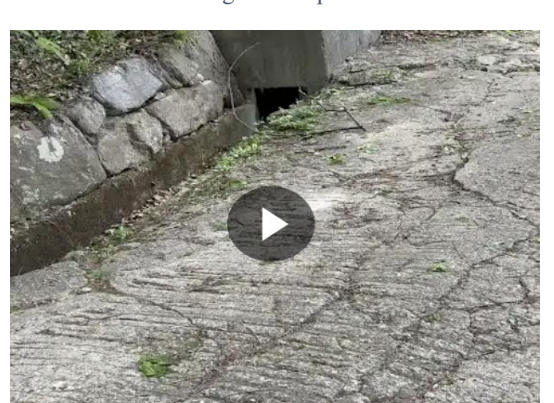


Fig. 11. Speed at Low Gear (video)



Fig. 13. <u>High Torque at Low Gear</u> (video)



Fig. 15. Overcoming Obstacle in Low Gear (video)

Fig. 8. Suspension Functioning (video)



Fig. 10. Measuring the COM



Fig. 12. Speed at High Gear (video)



Fig. 14. Flipping in High Gear (video)



Fig. 16. Wheel Slipping in High Gear (video)



Fig. 17. Disassembly



Fig. 18. Components



Fig. 19. Key element of tire fixation



Fig. 20. Uninflated tires

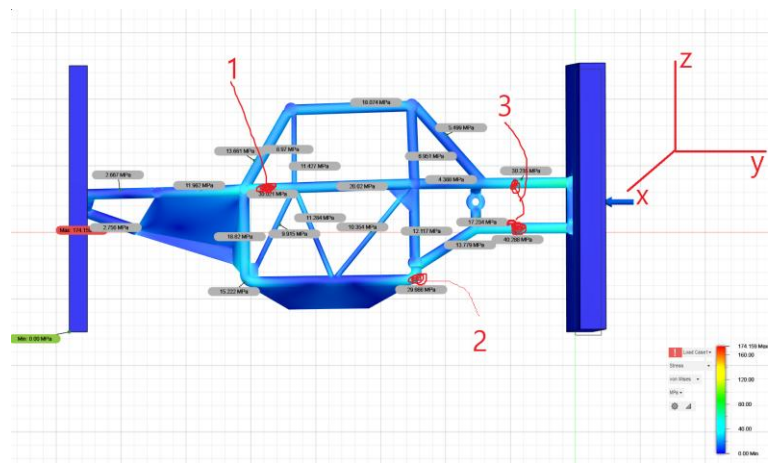


Fig. 21. Horizontal Load Analysis

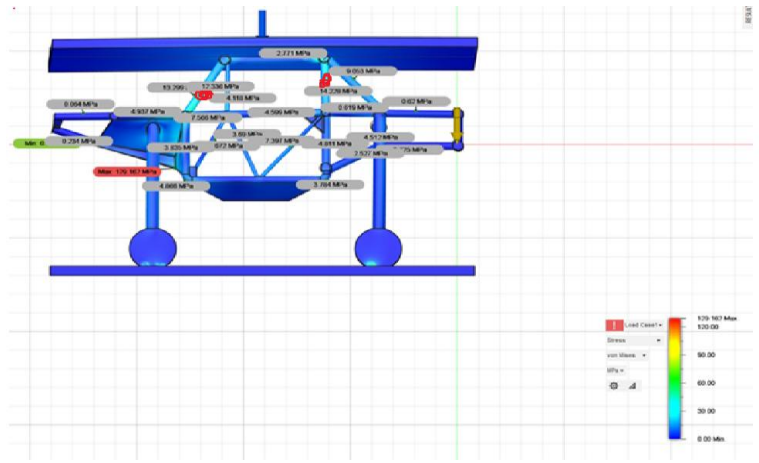


Fig. 22. Vertical Load Analysis

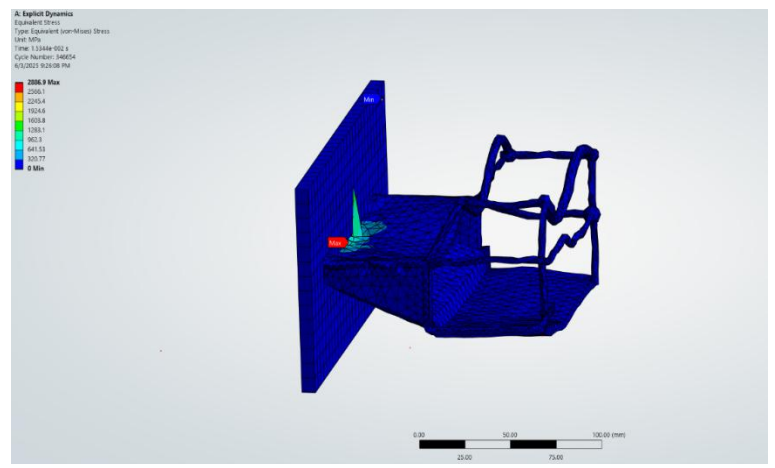


Fig. 23. Ansys Dynamic Simulation Result-Equivalent Stress

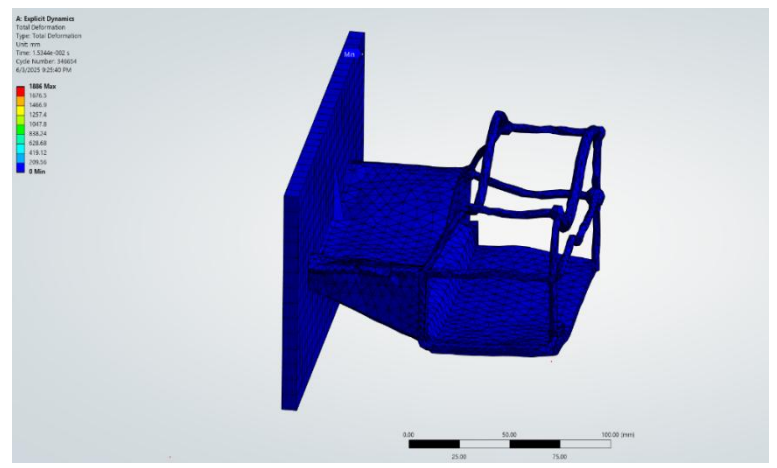


Fig. 24. Ansys Dynamic Simulation Result-Total Deformation

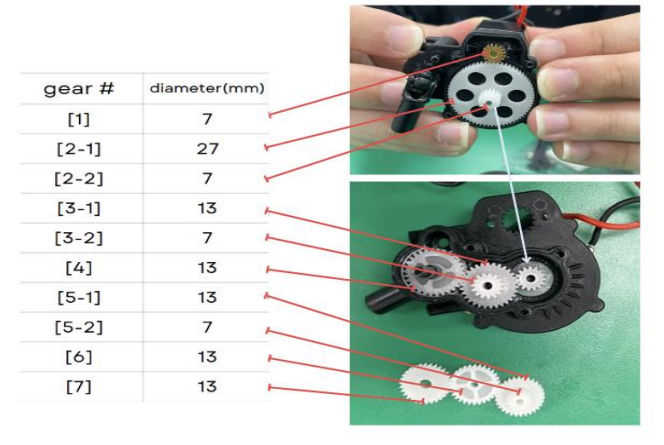


Fig. 25. Identification and diameter of gears in gearbox

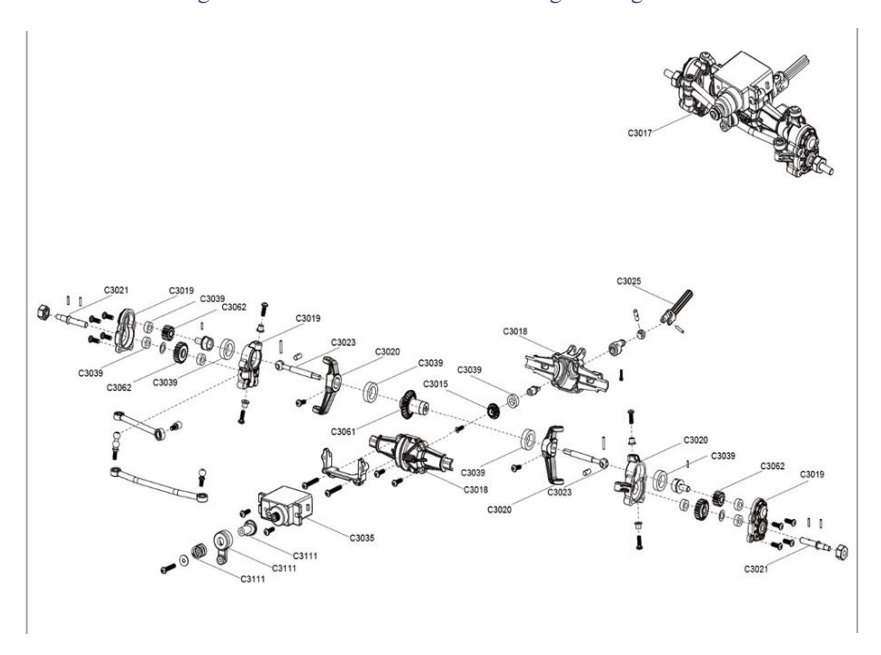


Fig. 26. Steering System exploded view



Fig. 27. Steering System Operation (video)



Fig. 28. Helically Contoured Servo Tip



Fig. 29. Helically Contoured Joint

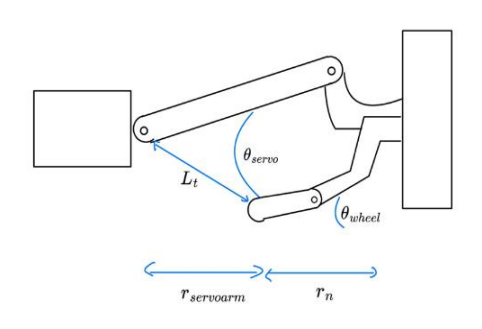


Fig. 31. Steering Mechanism

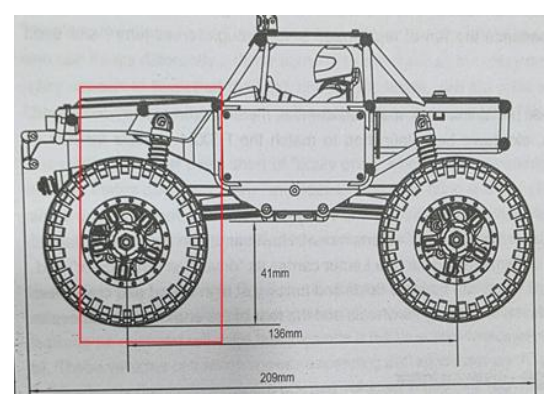


Fig. 33. Single Suspension System



Fig. 30. Self-centering steering mechanism (video)

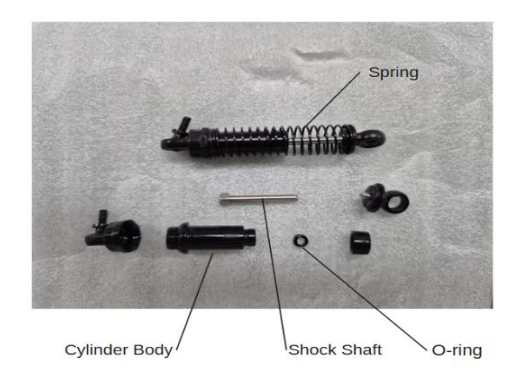


Fig. 32. Suspension Components

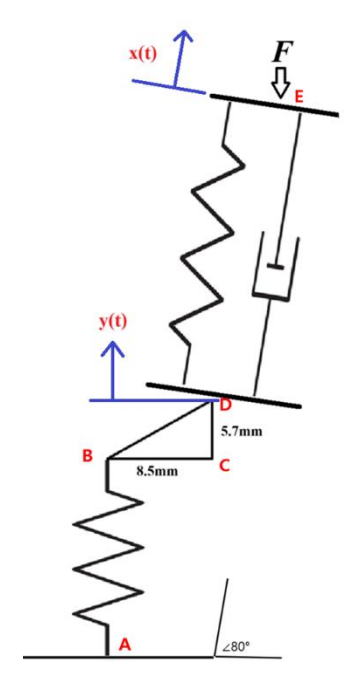


Fig. 34. Suspension System Modeling

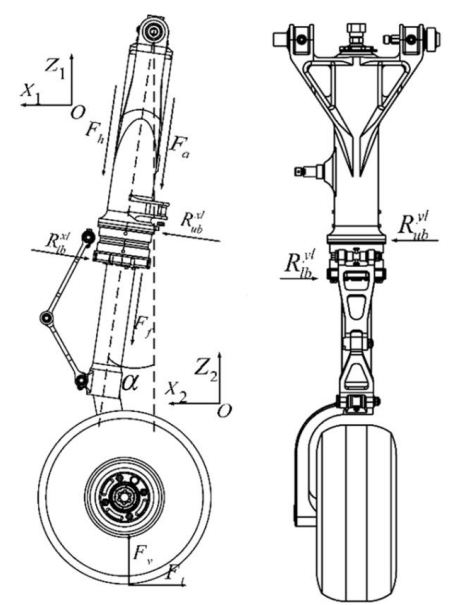


Fig. 35. Forces on the landing gear (source: DING, Yong Wei, et al.)



Fig. 37. Measuring Tire's Stiffness Value

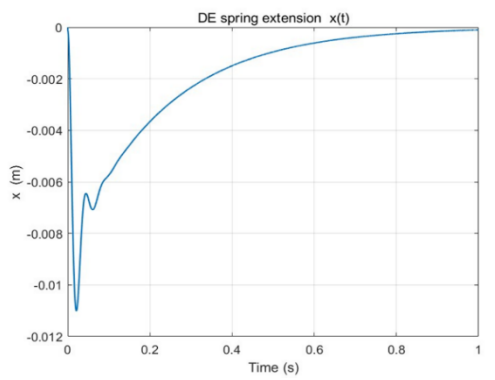


Fig. 39. Spring Extension-Time

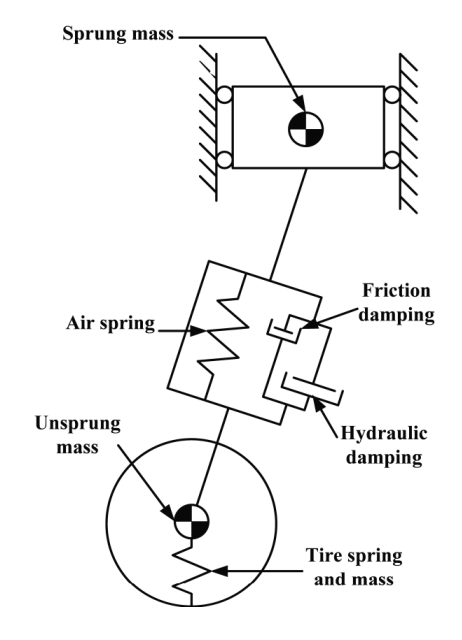


Fig. 36. System with two degrees of freedom (source: DING, Yong Wei, et al.)



Fig. 38. Measuring Damping Coefficient

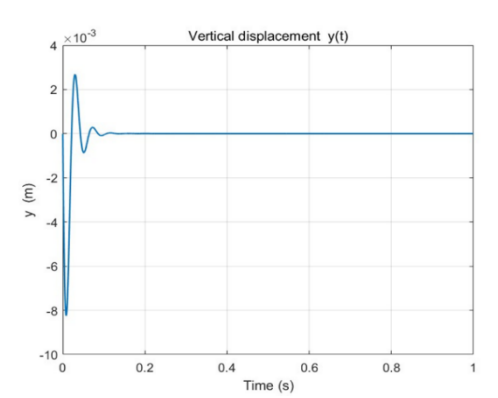


Fig. 40. Vertical Displacement-Time

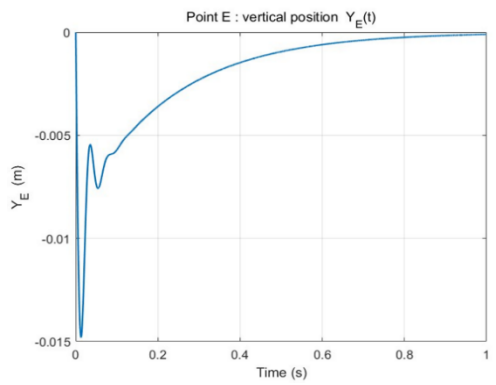


Fig. 41. Point E vertical Position-Time

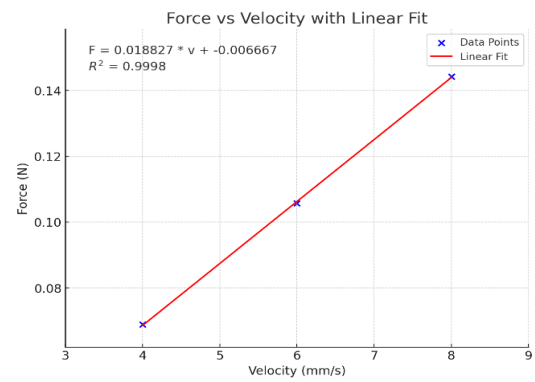


Fig. 43. Force-Velocity of Fabricated Damper



Fig. 42. Mixing Two Suspension Oils

# 2. Tables

	Diameter(mm)
[1]	7
[2-1]	27
[2-2]	7
[3-1]	13
[3-2]	7
[4]	13
[5-1]	13
[5-2]	7
[6]	13
[7]	13

Table. 1. Gear Number and Diameter

Sequence	[1]	[2-1]	[2-2]	[3-1]	[4]
Diameter	7	27	7	13	13
RPM ratio	27	7	7	$\frac{49}{13}$	$\frac{49}{13}$

Table. 2. Sequence in High Gear

Sequence	[1]	[2-1]	[2-2]	[3-1]	[3-2]	[5-1]	[5-2]	[6]	[7]
Diameter	7	27	7	13	7	13	7	13	13
RPM ratio	27	7	7	$\frac{49}{13}$	$\frac{49}{13}$	$\frac{7^3}{13^2}$	$\frac{7^3}{13^2}$	$\frac{7^4}{13^3}$	$\frac{7^4}{13^3}$

Table. 3. Sequence in Low Gear

Steering Ratio Characteristics		Driving Behavior	
Low (< 6)	Wheels respond very sensitively	Quick direction change, unstable at high speeds	
Medium (12~18) Typical for passenger vehicles		Precise and stable steering	
High (> 20) Wheels respond slowly		Maximized stability, suitable for large vehicles	

Table. 4. Relation Between Steering Ratio and Driving Behavior

Metric	Equation & result	Engineering guideline	Interpretation
Overshoot	$M_p = e^{-\frac{\pi \zeta}{\sqrt{1-\zeta^2}}} = 0.14$	$\leq$ 20 % to avoid	Well within the preferred band,
	$M_p = e^{-\sqrt{1-\zeta^2}} = 0.14$	noticeable bumps in ride	so passengers should not feel a
		comfort or steering	sharp "kick" when the
		response	suspension rebounds.
2% Settling time	4 - 0.076 a	$\leq 1$ s for automotive	Vibrations die out in roughly
	$t_s \approx \frac{4}{\zeta \omega_n} = 0.076 \mathrm{s}$	suspension	0.08 s—an order of magnitude
	, ,,		faster than the usual comfort
			threshold.
Logarithmic	$\delta = \frac{2\pi\zeta}{} = 2.26$		After a single oscillation period,
decrement	$o = \frac{1}{\sqrt{1 - 7^2}} = 2.26$		the displacement amplitude falls
	$rightarrow e^{-2.26} = 0.104$		to about 10 % of its initial value

Table. 5. Suspension Performance Metrics & Evaluations

#### 3. Derivation and Calculation

#### 3.1. Small Motion, Fixed 80° model

-Parameters

$$c_0$$
=20 Ns/m,  $k_1$ =87.77 N/m,  $k_2$ =2141 N/m,  $m$ =0.0875 kg

$$\zeta \approx 0.338$$
,  $\omega_n \approx 156 \text{ rad/s}$ 

-Eigenvalue

$$\lambda_1 = -7470.5, \qquad \lambda_2 = -52.64 + 146.87i, \qquad \lambda_3 = -52.64 - 146.87i, \\ \lambda_4 = -4.476$$

-Solutions

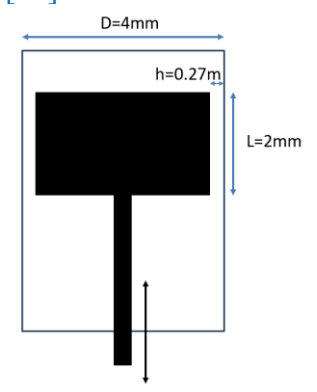
$$x(t) = 0.000138 e^{-7470.46t} - 0.00896 e^{-4.476t} + 0.00938 \cos(146.872t - 0.346) e^{-52.639t}$$

$$y(t) = 0.00000722 e^{-4.476 t} - 0.000135 e^{-7470.46 t} + 0.01365 \cos(146.872 t + 1.561) e^{-52.639 t}$$

## 3.2. Determination of Damper Oil Viscosity for a Target Damping Coefficient

This section presents a theoretical model for a single-acting piston-type damper in which fluid flows through the annular gap between the piston (valve) and the cylinder wall. The objective is to derive an expression relating the damping coefficient to the fluid viscosity and the damper geometry, and then calculate the required oil viscosity to achieve a target damping coefficient of  $c_0 = 18 \text{ N} \cdot \text{s/m}$ .

The modeling and calculation process was carried out with reference to the relevant literature. [14]



- Damper Geometry and Nomenclature
  - Cylinder internal diameter: D = 4 mm = 0.004 m
  - - Cylinder internal radius:  $R_0 = D/2 = 2 \text{ mm} = 0.002 \text{ m}$

The piston (valve) nominal area was measured to be about 75% of the cylinder area.

- Piston (valve) nominal area:  $A_p = 0.75$  Acyl, where Acyl =  $\pi R_0^2$
- $\bullet \qquad A_p = 0.75 \times \pi \times (0.002)^2 = 9.4248 \times 10^{-6} \ m^2$

Annular gap area (the leakage area between piston and cylinder wall):

• A gap = Acyl -  $A_p = 0.25 \text{ Acyl} = 0.25 \pi R_0^2$ 

Effective inner radius of piston (valve):

•  $R_i = \sqrt{0.75} \times R_o = \sqrt{0.75} \times 0.002 \approx 0.001732 \text{ m}$ 

Annular gap height:

•  $h = R_o - R_i = 0.002 - 0.001732 = 0.000268 \text{ m} \ (\approx 0.268 \text{ mm})$ 

Effective flow "width" (circumference at radius R<sub>i</sub>):

•  $W = 2\pi R_i = 2\pi \times 0.001732 \approx 0.01088 m$ 

Piston (valve) thickness, i.e., fluid flow length:

- L = 2 mm = 0.002 m
- -Viscous Flow in the Annular Gap (Poiseuille Approximation)

When the piston moves axially at velocity v, it induces oil flow through the narrow annular gap h, approximated by flow between two parallel plates of gap h, width W, and length L. Under laminar, incompressible conditions, the volumetric flow rate Q through such a gap subject to a pressure drop  $\Delta P$  is given by:

$$Q = (W h^3) / (12 \mu L) \cdot \Delta P$$
 (1)

On the other hand, the piston's displacement at speed v forces oil volume out at a rate:

$$Q = A_{\rm p} v \quad (2)$$

Equating (1) and (2) yields an expression for the pressure drop  $\Delta P$  across the valve:

$$\Delta P = (12 \,\mu \,L \,A_{\rm p} \,v) / (W \,h^3)$$

- Damping Force and Linear Damping Coefficient

The viscous damping force F acting on the piston is the pressure drop  $\Delta P$  multiplied by the piston effective area  $A_p$ :

$$F = \Delta P A_p = (12 \mu L A_p^2 / (W h^3)) v$$
 (3)

Because the force is proportional to velocity v, we identify the linear damping coefficient c as:

$$c = 12 \,\mu \,L \,A_{\rm p}^{2} / (W \,h^{3})$$
 (4)

- Calculation of Required Dynamic Viscosity µ

We wish to choose an oil whose viscosity  $\mu$  yields a damping coefficient of  $c_0 = 18$  N·s/m. Rearranging (4) for  $\mu$  gives:

$$\mu = (c_0 W h^3) / (12 L A_p^2)$$

Substitute each known quantity:

 $c_0 = 18 \text{ N} \cdot \text{s/m}$ 

W = 0.01088 m

h = 0.000268 m

L = 0.002 m

$$A_p = 9.4248 \times 10^{-6} \text{ m}^2$$

Hence:

$$\mu \approx 1.77 \, Pa \cdot s$$

- Conversion to Kinematic Viscosity (cSt)

The kinematic viscosity  $\nu$  (in m<sup>2</sup>/s) is related to dynamic viscosity  $\mu$  by:

$$\nu = \mu / \rho$$

Measured density:  $\rho \approx 880 \text{kg/m}^3$ . Therefore:

$$v \approx 1.77 / 880 \approx 2.01 \times 10^{-3} \, m^2/s$$

Since  $1 \text{ m}^2/\text{s} = 10^6 \text{ cSt}$ , this corresponds to:

$$\nu \approx 2010 \, cSt$$

#### 4. References

- [1] CAD Monkeys, RC Car Crash Test Simulation ANSYS Explicit Dynamics Tutorial, YouTube, 2022. [Online]. Available: <a href="https://www.youtube.com/watch?v=WzePgAFLTUA&t=248s">https://www.youtube.com/watch?v=WzePgAFLTUA&t=248s</a>
- [2] The Engineering Guide, *How Explicit Dynamics Works in ANSYS | Explicit Dynamics Explained*, YouTube, 2023. [Online]. Available: <a href="https://www.youtube.com/watch?v=EhTO0">https://www.youtube.com/watch?v=EhTO0</a> ovhnA
- [3] lukeME, What Happens Inside the Material During a Crash? | Car Crash Simulation | ANSYS LS-DYNA, YouTube, 2021. [Online]. Available: <a href="https://www.youtube.com/watch?v=K4us5lz9pK0&t=203s">https://www.youtube.com/watch?v=K4us5lz9pK0&t=203s</a>
- [4] Dudley, D. W. (1991). Handbook of Practical Gear Design (2nd ed.). CRC Press.
- [5] Litvin, F. L., & Fuentes, A. (2004). Gear Geometry and Applied Theory (2nd ed.). Cambridge University Press.
- [6] RC4Wheels. (2022). How to calculate gear ratio for RC cars. Retrieved from <a href="https://www.rc4wheels.com/en/post/calculate-the-gear-ratio">https://www.rc4wheels.com/en/post/calculate-the-gear-ratio</a>
- [7] ZHY Gear. (2023). Gear Ratios and Efficiency in Spur Gear Systems: An In-Depth Analysis. Retrieved
- [8] TowerPro. SG90 9g Micro Servo Specifications. Electronicos Caldas. www.electronicoscaldas.com/datasheet/SG90.pdf. Accessed 5 June 2025.
- [9] "Steering System Design for Small Vehicles." SAE Technical Paper Series, SAE International.
- [10] S. S. Rao, Mechanical Vibrations, 6th ed. Upper Saddle River, NJ, USA: Pearson Education, 2017.
- [11] T. Shaqarin and B. R. Noack, "Enhancing mechanical safety in suspension systems: Harnessing control Lyapunov and barrier functions for nonlinear quarter car model via quadratic programs," Applied Sciences, vol. 14, no. 8, p. 3140, 2024, doi: 10.3390/app14083140.
- [12] C.-T. Chen, Analog and Digital Control System Design: Transfer-Function, State-Space, and Algebraic Methods. Fort Worth, TX, USA: Saunders College Publishing, 1993.
- [13] H. Dahmani, O. Pagès, and A. El Hajjaji, "Observer-based state feedback control for vehicle chassis stability in critical situations," *IEEE Transactions on Control Systems Technology*, vol. 24, no. 2, pp. 636–643, 2016, doi: 10.1109/TCST.2015.2439236.
- [14] DING, Yong Wei, et al. Discharge coefficient calculation method of landing gear shock absorber and its influence on drop dynamics. *Journal of vibroengineering*, 2018, 20.7: 2550-2562.